# Design and In-Orbit Performance of a 1U 1 Gbit/s Optical Communication Terminal

Niek Doelman, *Member, IEEE*, Gert Witvoet, *Member, IEEE*, Dick de Bruijn, Arjo Bos, Arnoud Delissen, Dong-Nhat Nguyen, Loes Scheers, Hedser van Brug, Robbert Voorhoeve, Kristiaan Broekens, Cornelis Willem Korevaar, and Floris van Kempen

*(Invited Paper)*

***Abstract*—A CubeSat-compatible optical communication terminal (CubeCAT) has been designed, manufactured, and tested in orbit. It achieves 1 Gbit/s data rate in downlink at low bit-error-rate ($\leq 10^{-6}$), has a 1U volume, 1.0 kg mass and 10.8 W power consumption. It is based on a compact and efficient optical architecture, a low mass and stable mechanical structure, a high performing and robust pointing control strategy and designed to be compliant with the CCSDS O3K standard, with Reed-Solomon 223/255 coding. For launch survival a dedicated enveloping suspension module has been realized. Being launched and onboard the NorSat-TD satellite, the CubeCAT terminal has established various successful in-orbit communication downlinks. Data from the optical ground stations TNO (The Hague, Netherlands), MeO (Grasse, France) and Izaña (Tenerife, Spain) have been analyzed and verify the CubeCAT design.**

***Index Terms*—Optical wireless communication, satellite downlink, low size, weight and power, pointing control, suspension module, in-orbit demonstration.**

## I. Introduction

SATELLITES carrying high-resolution instruments require ever-increasing data rates to transmit their data back to Earth. To overcome bandwidth limitations in the radio spectrum, a promising alternative is to benefit from the unlicensed bandwidth in the optical spectrum. Furthermore, optical wireless technology has the potential to require very low Size, Weight and Power (SWaP). Also, it is well suited in the context of highly secure communication and quantum key distribution (QKD). Laser communication systems with space terminals have been demonstrated and deployed in recent years for various link configurations, including geostationary orbit satellite relay services, low Earth orbit (LEO) network constellations, ground to satellite feeder links and data downlinks from LEO satellites to ground.

A small payload and thus a low SWaP communication terminal is very beneficial in the context of Earth Observation. In a Direct-to-Earth (DTE) link from a small satellite, high data volumes from remote sensing missions can be downloaded to ground. High data rates in DTE links are required given the limited connection time (typically a few minutes) between the overpass of a LEO-satellite with respect to an optical ground station (OGS). In particular, a very low SWaP communication terminal pays off as it supports the application of Cube satellites (CubeSats), which have volumes of 1 U up to 12 U; where 1 U represents a volume of 10 cm $\times$ 10 cm $\times$ 10 cm. The use of miniaturized satellites such as CubeSats leads to a major decrease of launching cost, and also components cost due to the reduced lifetime requirements. Secondly, in the context of Autonomous Aerial Vehicle (AAV) platforms the requirements on the terminal's SWaP features can be stringent; see e.g. [1] and [2]. Networks of High-Altitude Pseudo Satellites (HAPS), drones and links between those and satellites are foreseen to become a key part in the high-speed non-terrestrial communication network.

Focusing on the DTE application, the downlink data rate needs to be 1 Gbit/s or higher to enable a sufficient data volume over the limited connection time between a passing LEO satellite and a ground station. This amounts for instance to maximum $\sim 5$ min for a $500\,\mathrm{km}$ satellite orbit height. Furthermore, a low bit-error-rate (BER) is a prerequisite; for instance as low as BER $\leq 10^{-6}$ at data link layer with an ultimate target of Quasi-Error-Free. Weather conditions play a dominant role with respect to the availability of the DTE link, since clouds, fog and haze may reduce the visibility at the relevant wavelength such that the received irradiance is below threshold. Such adverse conditions may be mitigated by the use of ground station diversity and the terrestrial fiber network.

The development of low SWaP optical communication terminals for DTE links has been picked up by various teams worldwide [3]. One of the earliest demonstrator terminals - and first onboard a micro-satellite - is the Small Optical TrAnsponder (SOTA) developed by NICT and launched with the SOCRATES satellite in 2014 [4]. The SOTA terminal has a volume of 5.4 U, a weight of $5.9\,\mathrm{kg}$, and power usage below $40\,\mathrm{W}$. It

Received 15 June 2025; revised 24 November 2025; accepted 9 January 2026. Date of publication 2 February 2026; date of current version 30 January 2026. *(Corresponding author: Niek Doelman.)*

Niek Doelman and Gert Witvoet are with the Opto-Mechatronics department of TNO, 2628 Delft, The Netherlands, and also with the Control Systems Technology section of Eindhoven University of Technology, 5612 Eindhoven, The Netherlands (e-mail: niek.doelman@tno.nl).

Dick de Bruijn, Arjo Bos, Arnoud Delissen, Dong-Nhat Nguyen, Hedser van Brug, Robbert Voorhoeve, Kristiaan Broekens, Cornelis Willem Korevaar, and Floris van Kempen are with the Opto-Mechatronics department of TNO, 2628 Delft, The Netherlands.

Loes Scheers is with the Electromagnetic Signatures and Propagation department of TNO, 2628 The Hague, The Netherlands.

Color versions of one or more figures in this article are available at https://doi.org/10.1109/JSTQE.2026.3655556.

Digital Object Identifier 10.1109/JSTQE.2026.3655556

has demonstrated up to 10 Mbit/s downlinks and performed successful communication links with various ground stations worldwide. Recent activities at NICT aim at the development and in-orbit demonstration of CubeSOTA, onboard a 6 U CubeSat platform. The communication payload itself of 3 U aims at a 10 Gbit/s data-rate for downlinks to ground and inter-satellite links between LEO and GEO.

The German Aerospace Center (DLR) started the development of laser communication technology for small satellites with the launch of the OSIRISv1 and v2 terminals [5]. The successor is the OSIRIS4CubeSat terminal with a volume of only 0.3 U, a weight of $0.395\,\mathrm{kg}$ and a power consumption of $\sim 9$ W. It is demonstrated in the PIXL-1 mission which was launched in 2021. The downlink data-rate goes up to 100 Mbit/s.

A very high data-rate terminal named TBIRD has been developed by MIT Lincoln Laboratory, employing off-the-shelf 100 G transceivers, and was launched in 2022. The TBIRD payload has a volume of approximately 3 U and a weight of less than $3\,\mathrm{kg}$. Successful demonstrations of 200 Gbit/s downlinks from the PTD-3 CubeSAT in an orbit of $530\,\mathrm{km}$ to the $1\,\mathrm{m}$ aperture OCTL ground station have been reported in [6]. These downlink tests yielded an error-free data transfer of more than 4 TB in a single satellite pass. And Massachusetts Institute of Technology aims at demonstrating full duplex, high data rate cross-links in the CLICK mission. The CLICK-A terminal was deployed from the International Space Station (ISS) in 2022. It has a mass of less than $1.2\,\mathrm{kg}$ and a volume of 1.2 U. The CLICK-B/C terminals with 1.5 U, and $1.5\,\mathrm{kg}$ are expected to be launched in 2025 and aim at a data rate of 20 Mbit/s.

The *CubeSat Communication Active Terminal* (CubeCAT) [8] by TNO has been targeted as a generic CubeSat-compatible terminal, originally with no specific satellite or mission in mind. With the objectives of a 1U volume, an effective $1.0\,\mathrm{kg}$ mass and 1 Gbit/s download data rate, CubeCAT acquires a unique position on the map of contemporary CubeSat communication payloads; see Fig. 1. Whereas the highest bitrate has been demonstrated by the TBIRD Laser Communication Terminal (LCT), the CubeCAT terminal has demonstrated the highest bitrate given its small size, weight and power consumption.

For the in-orbit demonstration opportunity onboard the NorSat-TD satellite, a dedicated suspension module has been added to CubeCAT in order to survive the heavier than anticipated launch loads onboard the associated Falcon-9 launch platform. NorSat-TD with CubeCAT was launched in April 2023, and successfully went through commissioning and testing. The NorSat-TD satellite decayed on May 22, 2025. This paper will address the design details of CubeCAT, its performance analysis and the results from various in-orbit experiments towards three ground stations.

This paper is organized as follows. Section II addresses the main requirements for the CubeCAT system and shows an analysis of the optical power budget for a downlink from CubeCAT to ground under a low elevation angle. Section III gives details of the design of the optical, mechanical and communication aspects. The pointing challenges are discussed in Section IV. Results of laboratory testing and verification are given in Section V and Section VI contains the most prominent results from the in-orbit testing phase with CubeCAT onboard the NorSat-TD satellite. The paper is finalized with the concluding Section VII.

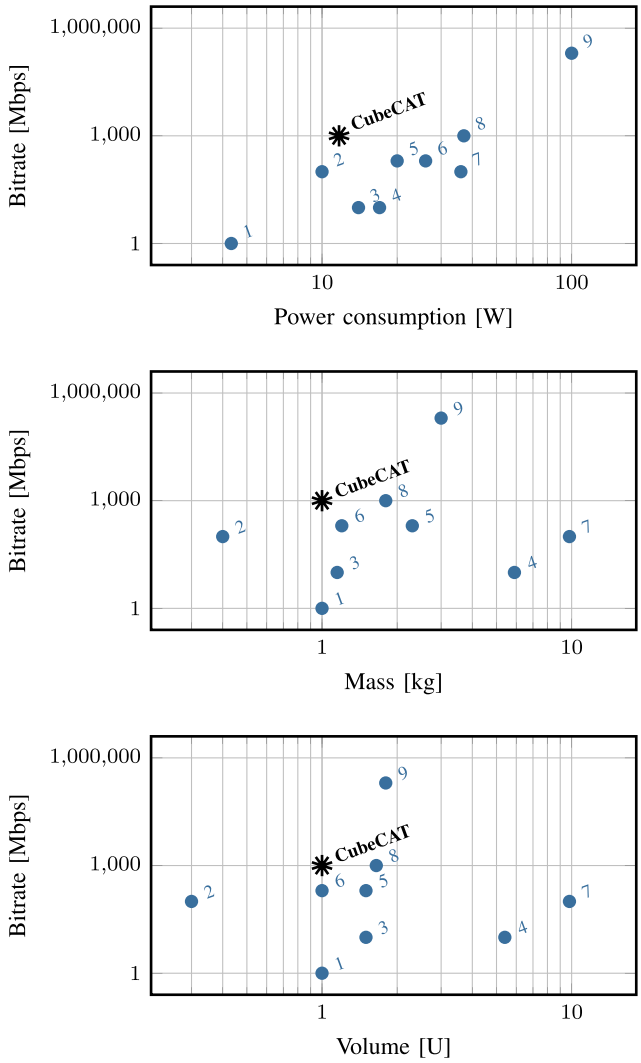


Fig. 1. Comparison of small laser communication terminals designed for DTE applications, launched and demonstrated in space [3], [7]: 1. VSOTA (NICT, not launched), 2. OSIRIS4CubeSat (DLR), 3. CLICK-A (MIT), 4. SOTA (NICT), 5. OSCD-B&C (Aerospace Corp.), 6. OSIRIS V1 (DLR), 7. SOLISS (SONY/JAXA, mounted on ISS), 8. OSIRIS V2 (DLR), 9. TBIRD (MIT Lincoln Laboratory) and CubeCAT (TNO/AAC). The bitrate is shown as a function of power consumption, mass and volume, respectively.

## II. CubeCAT System Requirements and Optical Link Analysis

The main challenge with the CubeCAT terminal is to design, manufacture and demonstrate in-orbit, a low volume, low mass, low power communication terminal, which is capable of achieving a high data-rate in DTE links for a LEO satellite. CubeCAT serves as a technology demonstrator system and it needs to comply with a set of key objectives, which are discussed below.

*Data Throughput and Storage* - The space terminal needs to achieve a downlink data rate of 1 Gbit/s towards a ground receiver with a BER of $\leq 10^{-6}$. This data rate signifies a competitive target for the demonstrator mission, also given the

volume of CubeCAT; see Fig. 1. A data rate of 1 Gbit/s allows for a substantial data-package to be off-loaded by CubeCAT during a total link time of several minutes within the satellite pass. Also, it is a clear improvement over current RF link performances. To comply with high resolution remote sensing missions, a capability to collect and store up to 128 Gbyte of user data is desirable. From a demonstrator perspective however, the on-board data storage functionality is considered non-critical and the emphasis is put on establishment of the optical link and the verification of the downlink BER via on-board generation of a pseudo-random sequence.

*Low Size, Weight and Power (SWaP)* - In order to fit onto small satellites, the terminal needs to utilize limited volume and power usage. Furthermore, from a demonstration perspective the use of optical communication wavelengths over RF-wavelengths allows for highly compact and low power solutions. The originally targeted volume for the space communication terminal is 1U, a maximum weight of $1.3\,\mathrm{kg}$ and power usage of at most $30\,\mathrm{W}$.

*Low Recurring cost* - To create a commercially viable technological solution, the cost versus bandwidth of the optical terminal needs to be comparable with the cost/bandwidth balance of existing RF systems. The targeted recurring production cost of the communication terminal has been quoted at maximum 50 kEUR (as of March 2020).

*Modularity* - A generic modular terminal with standard interfaces is required, such that it can be easily incorporated into a broad range of small satellites. This implies for instance a standard volume, acceptable mass and power usage and compliance with CCSDS communication standards. This objective also includes a wide range of satellite orbits (between 300 and 900 km), link ranges up to $1200\,\mathrm{km}$ and link acquisition for elevation angles larger than $20^\circ$. Furthermore, the in-orbit lifetime of the terminal needs to be at least 4 years.

*Space conditions* - The terminal needs to operate in and survive space environmental conditions. This implies a temperature range of $-20\,^\circ\mathrm{C}$ up to $+40\,^\circ\mathrm{C}$, a thermal gradient up to $5\,\mathrm{K}$, space environmental pressure and humidity levels, and a radiation dose up to 20 krad (at LEO orbit). Moreover, survival of launch vibrations and shock is imperative. Note, that the specific launch requirements are carrier dependent; see also Section III-B.

The selected system architecture for the CubeCAT terminal consists of five subsystems with the following functionalities:

- *Optical Bench*; guidance of the Tx downlink beam and the incoming beacon beam.
- *Fine-Steering Mirror* (FSM) with driver; steering of the Tx beam and pointing of Rx beam on the detector. The fine-steering mirror is located on the optical bench.
- *Laser source* with driver; generation of Tx beam.
- *Quad-cell sensor*; detector for fine-pointing of the beacon beam.
- *Processing unit*; CubeCAT controller of FSM, laser source and communications module.

All subsystems are mechanically contained within the CubeCAT structure. A diagram of the CubeCAT architecture with interfaces is depicted in Fig. 2. The selected laser source has $0.3\,\mathrm{W}$ power and generates a Tx beam at a wavelength $\lambda$ of

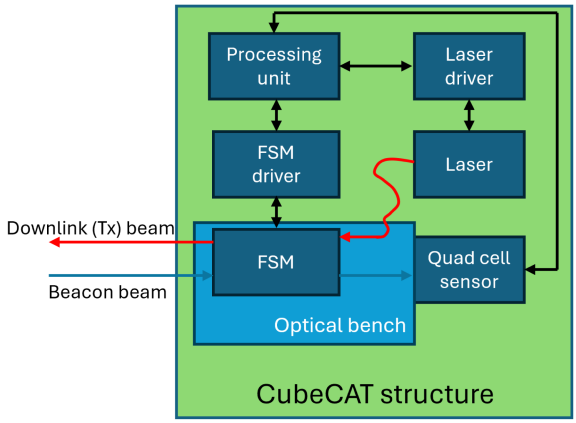


Fig. 2. Block diagram of CubeCAT subsystems; black lines indicate electrical connections, blue lines indicate the beacon beam, red lines indicate the downlink (Tx) beam and the red curved line indicates the optical fiber between the laser and the optical bench.

$1545\,\mathrm{nm}$. The aperture of the CubeCAT optical telescope is limited to $17\,\mathrm{mm}$. The fine steering mirror [9] used in CubeCAT is a TNO-designed mechanism [10], [11] using a variable reluctance actuator concept. It is capable of applying mechanical tip/tilt on a $20\,\mathrm{mm}$ diameter flat mirror.

### A. Channel Distortions

The free-space optical channel encompasses the optical path between the Satellite and Ground Station; more precisely from the CubeCAT exit pupil down to the ground telescope entrance pupil. The channel is susceptible to atmospheric distortions, potentially leading to a reduced communication performance. In the design of the CubeCAT terminal and the link budget, the relevant atmospheric disturbances have been specified as shown here.

*Atmospheric attenuation* - for the DTE link case a scenario with no clouds and a (horizontal) visibility of $23\,\mathrm{km}$ has been assumed.

*Sunlight scatter* - for this type of noise signal a sky radiance value of $0.02\,\mathrm{Wm^{-2}/sr/nm}$ has been assumed for the wavelength of interest.

*Earth radiance* - for a white, diffuse scene an Earth radiance value of $0.124\,\mathrm{Wm^{-2}/sr/nm}$ has been taken for the wavelength of interest.

*Atmospheric turbulence* - the Hufnagel-Valley 5/7 model (in e.g. [12]) for the profile of the refractive index structure constant $C_n^2$ has been adopted to assess the impact of optical turbulence on the wave irradiance scintillation.

### B. Channel Attenuation and Downlink Budget

The optical signal level at the receiver is determined by the optical source power and the total channel attenuation, of which most constituents have a deterministic character and two specific sources of attenuation – pointing jitter and atmospheric turbulence – are of a stochastic nature. Based on the principal

TABLE I
LINK BUDGET FOR THE SATELLITE-TO-GROUND LINK AT 20° ELEVATION

| *Parameter* | *value* | *unit* |
|---|---|---|
| Laser source power | 24.8 | dBm |
| Free space geometric loss | 47.6 | dB |
| Transmitter gain | 90.4 | dB |
| Free space range loss | 259.7 | dB |
| Receiver gain | 121.7 | dB |
| Space terminal | 2.6 | dB |
| Space terminal WFE loss | 0.9 | dB |
| Space terminal transmission loss | 1.2 | dB |
| Space terminal aperture decenter loss | 0.5 | dB |
| Atmospheric attenuation | 2.1 | dB |
| Pointing loss | 3.9 | dB |
| Average pointing loss | 0.9 | dB |
| Pointing jitter, 0.1st percentile | 3.0 | dB |
| Atmospheric fading, 0.1st percentile | 1.3 | dB |
| Received power | -32.7 (33.3) | dBm |

system design choices and the channel distortions, the attenuation factors are discussed in detail and quantified in a link budget overview, as shown in Table I. Here, the link attenuation is analyzed for a satellite orbit of $500\,\mathrm{km}$ and the challenging condition of $20^\circ$ elevation angle. Although the CubeCAT terminal needs to be versatile and capable of communicating with various ground stations worldwide, in order to analyze the link feasibility a 'model' ground receiver is used with an aperture of $0.6\,\mathrm{m}$ and a detector sensitivity of $1.49\,\mu\mathrm{Wm}^{-2}$.

For the free-space geometric loss analysis, the transmitter gain $GT_x$ including the effects of beam clipping and obscuration, is based on the analysis in [13]. For a beam waist radius $w_0$ and a wavelength $\lambda$, the transmitter gain equals $GT_x = 4(\pi w_0/\lambda)^2 g_T$. In here, $g_T$ is a correction factor that accounts for the clipping of the Gaussian beam at the aperture boundaries. Note that the CubeCAT telescope has no central obscuration (see Section II-I-A). Then with $w_0 = 7.6$ mm and $\lambda = 1545$ nm a $GT_x$ of 90.4dB is obtained. The free-space range loss is based on a $1190\,\mathrm{km}$ link which applies to an elevation of $20^\circ$ and a satellite orbit of $500\,\mathrm{km}$ and the receiver antenna gain is based on a $0.6\,\mathrm{m}$ ground station aperture.

Opto-mechanical inaccuracies of the CubeCAT terminal itself lead to an additional loss of 2.6 dB; see also Section III-A. The atmospheric attenuation is based on MODTRAN calculations [14] for a visibility range of $23\,\mathrm{km}$ and no clouds. The mean 2D radial pointing error at the CubeCAT terminal is estimated at $9.8\,\mu\mathrm{rad}$. Note, that the beam divergence angle is much larger as it equals $85.4\,\mu\mathrm{rad}$.

For the CubeCAT beam propagating through an atmospheric turbulent channel, substantial irradiance fluctuations in the receiver plane can be expected. For this downlink case, the variance of wave log-amplitude fluctuations $\sigma_\chi^2$ is evaluated on the basis of [12]:

$$\sigma_\chi^2 = 4\pi^2 k_w^2 \int_0^L \int_0^\infty \kappa \Phi_n(\kappa, z) \sin^2\left(\frac{\kappa^2 z}{2k_w}\right) G_A(\kappa, D) dz d\kappa \tag{1}$$

in which $k_w$ equals $2\pi/\lambda$, $L$ is the slant range, $\kappa$ is the scalar transverse wavenumber, $z$ is the axial co-ordinate and $\Phi_n(\kappa, z)$ stands for the spectrum of refractive index fluctuations. The function $G_A$ represents the effect of receiver aperture averaging and equals $G_A(\kappa, D) = [4J_1(\kappa D/2)/\kappa D]^2$, in which $D$ is the aperture diameter of the ground station telescope. Note that in the weak fluctuations regime the scintillation index of irradiance $\sigma_I^2$ follows from $\sigma_I^2 = \exp(4\sigma_\chi^2) - 1$.

For atmospheric turbulence modeled by the Hufnagel-Valley 5/7 $C_n^2$-profile, and the von Kármán power spectral density with outer scale $30\,\mathrm{m}$, a CubeCAT downlink to sea level gives an on-axis scintillation index of up to $\sigma_I^2 = 1.1$ for $20^\circ$ elevation. However, as a result of aperture averaging by the ground station telescope, on the basis of (1) an effective scintillation index of 0.05 is encountered. This index is used to assess the probability distribution of the link attenuation caused by atmospheric turbulence. For the beacon uplink path from OGS to CubeCAT a similar analysis can be made for the optical power budget. An example of this is given in Section VI for the TNO OGS.

The two stochastic factors - pointing jitter and log-amplitude fluctuations - require an integrated approach. Based on the work in [15] and [16], the overall probability distribution of irradiance can be evaluated. In the presence of a pointing boresight displacement $s$, the probability density function is represented by [16]:

$$P_I(I) = \frac{\gamma^2 \exp(u_a)}{2I_0^{\gamma^2}} I^{\gamma^2 - 1} \operatorname{erfc}\left(\frac{\ln(\frac{I}{I_0}) + u_b}{2\sqrt{2}u_c}\right) \tag{2}$$

in which $I_0$ denotes the irradiance at the receiver in the absence of pointing error loss and atmospheric fading loss. In (2), $\gamma = w_z/2\sigma_s$ is the ratio between the equivalent beam radius $w_z$ and the standard deviation of the pointing jitter-induced displacement $\sigma_s$, both in the receiver plane, and the factors $u_a$, $u_b$ and $u_c$ are defined as

$$u_a = \frac{s^2}{\sigma_s^2} + 2\sigma_\chi^2\gamma^2(1+\gamma^2), \tag{3a}$$

$$u_b = \frac{6s^2}{w_z^2} + 2\sigma_\chi^2(1+2\gamma^2), \tag{3b}$$

$$u_c = \sqrt{\frac{4s^2\sigma_s^2}{w_z^4} + \sigma_\chi^2}. \tag{3c}$$

The underlying probability distribution for irradiance scintillation has the log-normal form, based on the observation that the scintillation index is low (0.05 for elevation $20^\circ$). With an overall root-mean-square pointing error of 11 $\mu$rad (see Section IV for further details), the probability distribution of the received irradiance is represented in the top graph of Fig. 3. It indicates the mean irradiance level and the relatively large degree of fluctuations. In Fig. 3 also the case of the maximum elevation angle of $90^\circ$ is depicted. This clearly illustrates the variation in both mean irradiance and irradiance fluctuations with elevation angle. Further analysis of the transient behavior of the probability distribution of irradiance with satellite motion can be found in [17].

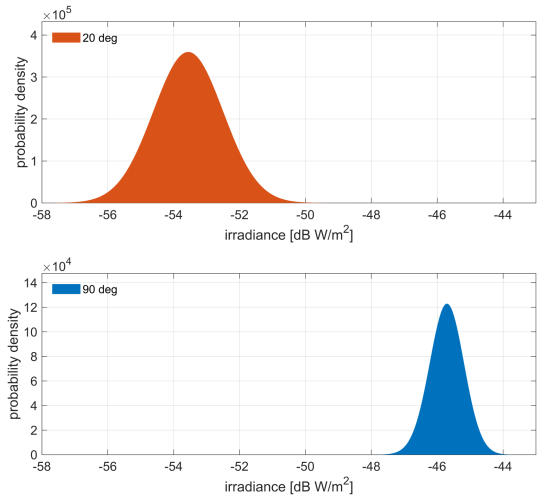


Fig. 3. Probability density of received irradiance for a unit power source for the CubeCAT downlink at 20° and 90° elevation angles.

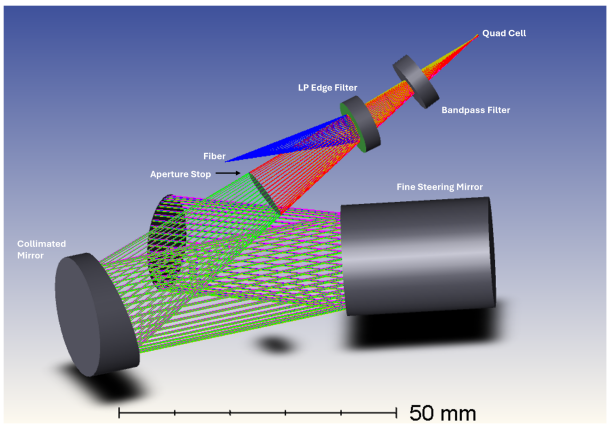


Fig. 4. Layout of the CubeCAT optical path with key elements.

## III. CubeCAT Terminal Design Analysis

This section discusses the optical, mechanical and communication design aspects of the CubeCAT terminal in further detail.

### A. Optical Design

The optical design of the CubeCat terminal is driven by two main requirements: low volume and low recurring cost. The selected approach is to use a minimum number of optical and mechanical elements. Fig. 4 shows the resultant optical architecture with both the transmitter (Tx) and receiver (Rx) beam paths. The system is basically a single off-axis parabola with some flat optics for beam directing and wavelength selection. The Tx path initiates at the laser fiber source, with wavelength $\lambda = 1545\,\mathrm{nm}$. The beam is reflected by the Long Pass (LP) edge filter. This filter reflects the shorter and transmits the longer wavelengths. Then, the beam passes through the aperture stop and is collimated by the parabolic mirror. Finally, the beam is reflected by the fine steering mirror (FSM), which has a optical angular range. The optical bench also needs to receive light, with the Rx channel operating at $1590\,\mathrm{nm}$. The FSM positioned in front of the parabolic mirror is tuned to have the Rx angle of incidence close to the optimal angle for high optical performance. After reflection by the parabolic mirror the Rx beam passes through the LP filter, a band-pass filter and impinges on a quad-cell (QC). The quad-cell is used as a tracking sensor to return angular pointing information to the FSM control loop. It is also capable to detect a 200 kBaud uplink signal, and as such the QC expects a $100\,\mathrm{kHz}$ beacon. Note however, that due to time constraints the data uplink demodulation has not been implemented in the in-orbit tests. The band-pass filter in front of the QC blocks out-of-band light from the measured signal.

The focal length of the parabolic collimator mirror is determined by the Mode Field Diameter (MFD) of the Tx fiber, the cut-off ratio of the Gaussian beam and the pupil size of the system. Based on an MFD at a wavelength of $1545\,\mathrm{nm}$ of $10.4\,\mu\mathrm{m}$, and cut-off at 1.12 times the $1/e^2$ Gaussian beam width [13], the stop size is found to be $9.6\,\mathrm{mm}$ at a distance of $45\,\mathrm{mm}$ from the fiber. The exit beam size needs to be $17\,\mathrm{mm}$, which results in an effective focal length of the parabolic mirror of $80.4\,\mathrm{mm}$ for the $6.1°$ Gaussian beam angle. The Rx beam light passes through a tilted LP filter, which leads to astigmatism for a focusing beam and thereby a rotational non-symmetric beam spot. To overcome this effect the band filter is also tilted to restore the rotational symmetry of the beam spot. The QC signal is used for control of the FSM and for proper performance this cell is positioned about $1\,\mathrm{mm}$ behind the focal point of the parabolic mirror.

As a result of the limited number of optical components, the wavefront error (WFE) can be relatively low ($\leq 100\,\mathrm{nm}$). The as-designed optical system is aberration-free for the Tx channel, allowing ample room for alignment and production errors. Once the system is aligned for the Tx channel, i.e. a collimated output beam with diffraction limited wavefront error is established, the Rx channel only needs to be adjusted to arrive at the QC with a rotationally symmetric spot with the correct size.

The parabolic mirror is produced by diamond turning and therefore can have a periodic, spatial structure, leading to the so-called mid-spatial frequency errors. Since it is an off-axis mirror, the structure will consist of approximately straight lines, resulting in diffraction orders. Analysis has shown that merely the periodic structures between 2 and 0.5 lp/mm will interfere with the signal on the QC. As long as the amplitude is below $20\,\mathrm{nm}$ (PV), this effect can be neglected. Analyses of stray light and ghosting indicate that the measures taken, i.e. unwanted light suppression by an OD 5 filter, both for the LP filter and the band-filter before the QC, is sufficient to restrict the impact of these effects. The laser transmitter consists of a directly modulated distributed feedback (DFB) laser with an integrated optical amplifier, achieving a minimum extinction ratio of $3\,\mathrm{dB}$ under $1\,\mathrm{GHz}$ modulation and an optical output power range of $20\,\mathrm{mW}$ to $300\,\mathrm{mW}$.

### B. Mechanical Design

The driving requirements for the mechanical design of the CubeCAT terminal are (1) limited volume and weight, (2) low

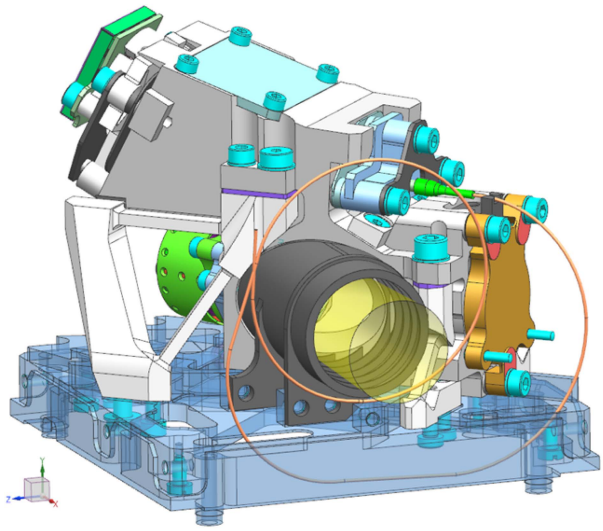

Fig. 5. CubeCAT optical bench mounted on its base-plate in a statically determined way. The rest of the sub-assemblies are omitted for clarity. The aperture is clearly visible at the end of the black baffle.

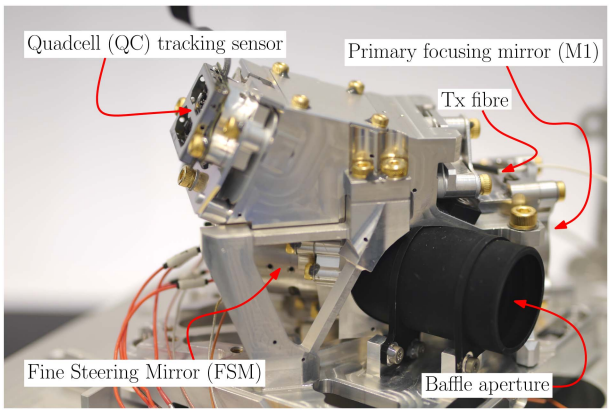


Fig. 6. Picture of the CubeCAT optical bench, highlighting some of the most important components.

link losses, (3) stability of alignment between Tx and Rx beam and (4) launch survival.

*1) Volume and Weight:* One of the main challenges is to fit the mechanical structure, the optical bench, the laser module, the fine steering mirror, and the electronics including cabling and connectors within the 1U volume. A solution has been found by the diagonal placement of the optical bench on the baseplate; see Figs. 5 and 6. The optical bench is mounted using 6 struts in a statically determined way, in order to minimize stresses carrying over from the structure. Moreover, the laser module has to fit around the remaining volume, and therefore is designed to fit within an L-shaped volume. The FSM is mounted on the optical bench. Furthermore, also the low mass requirement for the 1U unit is driving the design towards a system mainly consisting of aluminum alloy parts.

*2) Low Link Losses:* The most stringent requirement on opto-mechanical alignment, is that the center of the beacon field-of-view (Rx beam) shall be aligned with the Tx beam within $\pm 0.3\,\mathrm{mrad}$ ($3\sigma$). This has been met by primarily relying on mechanical machining tolerances within the order of 5 to 10 $\mu$m.

*3) Stability:* The most challenging requirement for the optical bench is given by the stability of co-alignment of the Tx and Rx beam: this may not deviate more than 20 $\mu$rad ($3\sigma$ value) over time. From the stability budget it follows that lateral stabilities on a component level of approximately $300\,\mathrm{nm}$ and $6\,\mu\mathrm{rad}$ out-of-plane rotations are required. Compared to previous designs with extremely stable space equipment, namely the Optel-µ terminal in the TESLA-C project [18] and the ESA Gaia mission's Basic Angle Measurement (BAM) system [19], the CubeCAT requirements are significantly more challenging. Whereas the lateral stability of certain components in the Optel-µ terminal and Gaia BAM was required to be respectively $\leq 1.2\,\mu\mathrm{m}$ (bonded) and $\leq 0.97\,\mu\mathrm{m}$ (removable clamp), CubeCAT requires stabilities down to the aforementioned $0.3\,\mu\mathrm{m}$. Therefore, a novel concept has been introduced: the ceramic ferrule is mounted in the aluminum mount using a thermal shrink fit. A similar solution has been applied to the quad-cell.

To meet the stability requirements, extensive analyses including Structural-Thermal-Optical-Performance (STOP) analysis have been performed, resulting in a design with maximal a-thermal properties. The optical bench including all structural parts and the primary mirror, the supporting mounts, and the base structure have been manufactured from the same aluminum alloy. Furthermore, for each optical element thermal centers are created by integrating flexures into the mounts, which also minimizes effects of assembly and integration loads and eliminates friction and hysteresis. To minimize the heat load on the optical bench, the QC detection element is mounted directly on the optical bench. The remainder of the QC electronics is mounted on the CubeCAT structure.

*4) Launch Survival:* Driven by the modularity requirement, CubeCAT has been designed as a generic, versatile communication terminal that fits a 1U CubeSat volume. The opportunity of in-orbit testing onboard the NorSat-TD satellite however, has demanded a few design modifications, in particular with respect to the launch loads introduced by the Falcon-9 carrier of NorSAT-TD. It has been decided to keep the 1U CubeCAT terminal intact and add a suspension module around it. This enveloping vibration isolation structure has been designed specifically for the NorSat mission. It consists of a flexible mounting based on six damping struts to establish the first system eigenfrequencies around a specific value, while minimizing random vibration and shock loads on the CubeCAT module during launch [20]. This multi-material vibration isolation structure consists of tailor-designed geometries in which viscoelastic rubber is integrated into metal struts for hysteresis-free operation, increasing damping and thereby further reducing random vibration loads. Long-term drift and creep as well as outgassing are prevented due to the way the viscoelastic material is constrained and integrated. The specific shape of the struts has been realized by use of 3D printing technology.

The addition of the struts-based vibration damping cover might lead to poor thermal coupling from heat dissipated on CubeCAT to the platform. Thermal straps as a solution to restore the thermal coupling have been discarded as these would

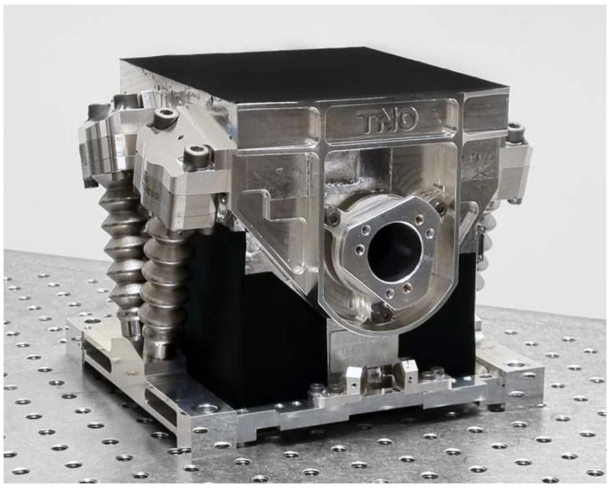


Fig. 7. The suspension module with the CubeCAT terminal.

undermine the suspension performance due to their inherent stiffness. Instead, a heat radiation solution has been selected by taping the overall system with coated black foil. The terminal's temperature is being monitored during operation to ensure it remains within its operational boundaries. A picture of the suspension module is given in Fig. 7. Together with the CubeCAT terminal it is also known as the 'SmallCAT' terminal.

### C. Communication Approach

The physical layer and data link layer of the CubeCAT to OGS link have been designed to maximize compliance with the CCSDS 141.x and 142.x standards. In particular, the (draft) optical on-off-keying (O3K) standard has been implemented with on-off-keying NRZ modulation, coding based on a Reed-Solomon 223/255 code and a downlink wavelength at $1545\,\mathrm{nm}$. A modem board developed by AAC Hyperion served as the actual hardware implementation in CubeCAT.

The uplink beacon is modulated with an alternating on-off-keying signal at 200 kBaud, without actual user data, at 1590 nm. In addition to O3K coding, also pseudo random binary sequences (PRBS) can be transmitted, and the results reported in this publication have been achieved with a PRBS23 sequence, generated with the polynomial: $x^{23} + x^{18} + 1$.

The TNO OGS in The Hague - $800\,\mathrm{mm}$ aperture, $45\,\mathrm{m}$ above sea level - is one of the test facilities with CubeCAT. For the in-orbit experiment towards this OGS, a free-space coupled high-speed optical-to-electrical converter is used, which consists of an avalanche photodiode (APD) detector, trans-impedance amplifier (TIA) and limiting amplifier (LIA). The converter is built into the optical bench, with its differential RF output ports accessible on the outside. The differential signals are then equally divided using RF power splitters to enable simultaneous analysis and cross-validation of the downlink signal quality by:

- a high-speed real-time oscilloscope for waveform storage, eye diagram analysis and offline decoding of BER,
- an in-house developed ground station modem with storage server, suitable for real-time decoding, data storage and relaying.

TABLE II
CONCISE OVERVIEW OF SYSTEM ENGINEERING POINTING BUDGETS

| Range | Description | Budget [µrad rms] | Total [µrad rms] |
|---|---|---|---|
| Low frequency | Satellite motion | 5 | 9.2 |
| | Quad-cell noise | 6.67 | |
| | Quad-cell non-linearity | 2.33 | |
| | Mechanical stability | 1.5 | |
| | FSM driver noise | 2 | |
| | Unforeseen / margin | 1.9 | |
| High frequency | Satellite motion | 5 | 6.0 |
| | Mechanical stability | 3 | |
| | Unforeseen / margin | 1.5 | |

## IV. Pointing Control Analysis and Design

One of the larger yet controllable contributors to the channel gain (Table I) is the pointing loss, which is largely affected by the pointing performance of the space terminal. Early in the development phase a dedicated pointing budget has been constructed, identifying possible pointing error sources and allocating budgets to them, of which a short overview is shown in Table II. A distinction has been made between low- and high-frequency error contributions, with a total of $11\,\mu\mathrm{rad}$ root-mean-square (rms), which is sufficient to meet the pointing loss requirement mentioned in Table I.

The CubeCAT terminal controls its Tx-pointing via active control of the Rx-angle, utilizing a common-path approach. The received Rx beam is focused onto a spot on the QC sensor. This spot location is a direct measure for the angular misalignment between the terminal boresight and the line-of-sight towards the ground station. By active feedback control of the spot location with the internal FSM, the Tx and Rx beams can be co-aligned. Compensation of the point-ahead angle (PAA) can be arranged by imposing the PAA offset with respect to the Tx/Rx aligned spot location on the QC in the feedback control loop. This approach avoids the need for a separate point-ahead mirror.[1] The quality of this co-alignment effectively determines the pointing loss, which is partly driven by static errors (including the static Tx/Rx-misalignment[2] between the Tx-fiber and the QC), and partly by residual dynamic errors propagating through the pointing feedback loop.

### A. Pointing Control Philosophy

The dynamic errors are predominantly determined by the vibrations induced by satellite motion, and the noise from the QC (see Table II). The pointing controller directly affects the propagation of these error sources, but in opposing ways: whereas sensor noise can be mitigated by lowering the feedback

[1]CubeCAT provides a software interface to receive orbital and attitude data from the spacecraft for its PAA calculations, expressed in the CubeCAT coordinate frame, which can be sent to the real-time processor roughly once per second.

[2]CubeCAT provides functionality to re-assess and set the Tx/Rx-alignment setpoint while in orbit, so as to correct for possible changes after launch.

control bandwidth, attenuation of (micro-)vibrations benefits from higher control bandwidths.

The amount of Rx-beacon light that CubeCAT receives will fluctuate heavily, due to for instance satellite motion, ground station pointing errors and atmospheric turbulence, and this directly affects the noise on the spot location calculation on the QC. Micro-vibrations are hard to quantify *a priori*, and often remain uncertain in the design phase. The budgets in Table II need to be met at all times though, including the worst-case scenario of maximum sensor noise. The selected design philosophy for the pointing controller is such that the attenuation of possible satellite-induced micro-vibrations is maximized, under the constraint that the sensor-noise induced pointing error remains just within the required $6.67\,\mu$rad rms for the worst case. Using this controller and the allowable budget of $5\,\mu$rad rms (both for low and high frequencies), a maximum amount of allowable satellite motion is then derived, which can be used later in communication with the satellite manufacturer to assess compliance. This design philosophy for pointing control will be further explained in the next sections.

### B. Tracking Sensor and Its Noise

The CubeCAT tracking sensor system comprises an off-the-shelf QC and custom-designed electronics. The latter mixes the analog signals of the four quadrants of the QC with an internal 100 kHz clock, to lock on the 200 kbps modulation of the Rx-beacon, and then combines, filters and down-samples these signals to generate 20 kHz tip $\theta_x$ and tilt $\theta_y$ information for the feedback loop, with as low latency as possible. This locking on the 200 kbps tone makes the sensor system relatively insensitive to DC background signals from e.g. sunlight and albedo. The spot on the QC is deliberately slightly out-of-focus to achieve an optimal balance between sensitivity and linearity of the QC response. Tests have revealed that the resulting total field-of-view (FoV) is about $\pm 6$ mrad. The central $\pm 0.6$ mrad behaves almost perfectly linear, with measured maximum non-linearities of $4.2\,\mu$rad in $\theta_x$ and $5.3\,\mu$rad in $\theta_y$, hence at most $6.8\,\mu$rad in total, which is compliant with the rms budget stated in Table II.

After calibration of the QC central-FoV read-out signal to actual Rx-beam angles using a theodolite, measurements have been taken to identify the noise level of the QC system. To this end, the QC has been exposed to various different intensities and along various nominal spot locations power spectra have been computed of the QC output, which were all by approximation flat. From these spectra the sensor noise floor has been estimated, expressed in angular noise at the terminal output, the summary of which is presented in Fig. 8, clearly showing an inversely proportional relation between received intensity and angular noise. The QC system is explicitly designed to operate at power levels between 0.8 nW and 300 nW. Near these edges the noise is somewhat higher due to under- and over-illumination of the QC, but still within the operational requirement defined for the QC system.

The pointing budgets in Table II should hold for powers down to 0.8 nW. The highest observed sensor noise level is

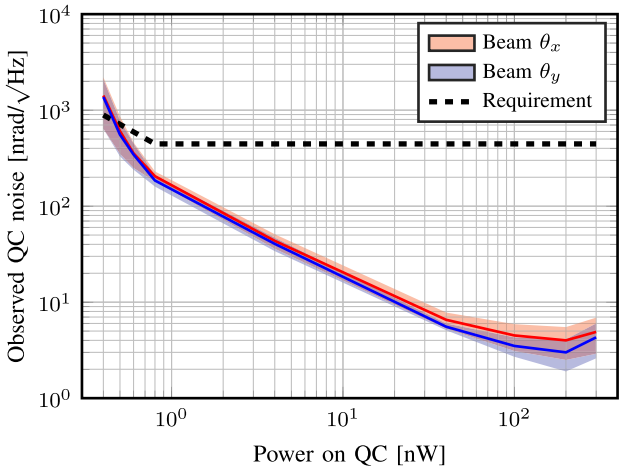


Fig. 8. Observed QC noise as a function of laser power (intensity) on the QC; the shaded areas indicate the spread along several measurements for each power in both tip $\theta_x$ (red) and tilt $\theta_y$ (blue), partly due to QC non-linearities, but predominantly due to measurement uncertainty.

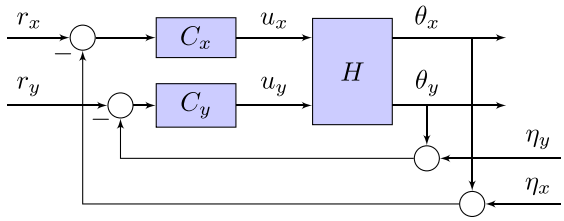


Fig. 9. Decoupled tip/tilt feedback loop, including sensor noise $\eta_x$ and $\eta_y$. The true pointing is indicated by $\theta_x$ and $\theta_y$, while $u_x$ and $u_y$ represent the requested tip/tilt torques of the FSM. The reference signals for $\theta_x$ and $\theta_y$ are indicated by $r_x$ and $r_y$ respectively.

230 nrad/$\sqrt{\text{Hz}}$ for this case; this value, plus 20% margin, is subsequently taken as input to the controller design process.

### C. Controller Design

The control architecture deployed in CubeCAT is schematically represented in Fig. 9. It uses a decoupled approach, with two independent single-input-single-output (SISO) tip and tilt controllers $C_x$ and $C_y$, assuming negligible interaction between these axes in the plant $H$. The true tip/tilt pointing angles are indicated by $\theta_x$ and $\theta_y$, the measurement of which is disturbed by the sensor noise $\eta_x$ and $\eta_y$.

The propagation of sensor noise to the power spectral density (PSD) of the actual pointing error is, when ignoring possible interaction in the plant $H$, given by

$$P_{\theta_i}(f) = |T_i(f)|^2 \, P_{\eta_i}(f), \tag{4}$$

with $T_i(f)$ the frequency response of the closed-loop transfer function $T_i(s)$:

$$T_i(s) = \frac{H_{ii}(s)C_i(s)}{1 + H_{ii}(s)C_i(s)}, \tag{5}$$

where $i$ denotes either the tip $x$ or tilt $y$ axis, $H_{ii}$ represents the corresponding diagonal element of $H$, and $P_{\eta_i}(f)$ and $P_{\theta_i}(f)$

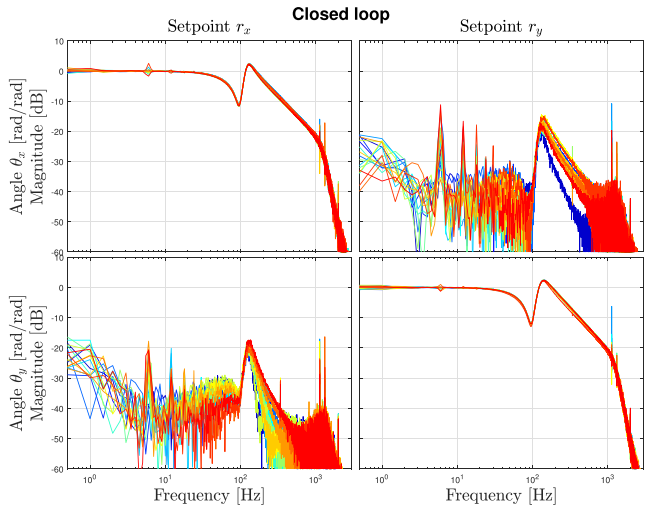


Fig. 10. Designed frequency responses of the closed-loop $T$, using actual plant measurements; different colors represent different plant frequency response functions measured along various nominal QC positions.

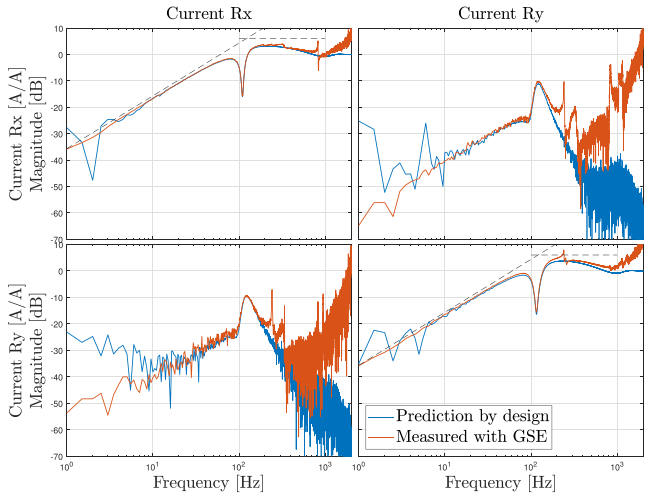


Fig. 11. CubeCAT closed-loop attenuation performance of angle-of-arrival angles at aperture, both by design (blue), and by explicit experimental verification (red) using the setup in Fig. 12.

denote the PSDs of the sensor noise and pointing angle respectively. As mentioned in Section IV-B, $P_{\eta_i}(f)$ is approximately flat, meaning that

$$P_{\eta_i}(f) \approx K_\eta^2 \qquad \forall f \in [0, f_s/2], \tag{6}$$

where $K_\eta \leq 276$ nrad/$\sqrt{\text{Hz}}$ and $f_s$ is the sample rate. The rms pointing jitter can then be written as

$$\theta_{\eta_i}^{\text{rms}} = \sqrt{\int_0^{f_s/2} P_{\theta_i}(f)\,\mathrm{d}f} = K_\eta \cdot \sqrt{\int_0^{f_s/2} |T_i(f)|^2\,\mathrm{d}f}$$
$$= \sqrt{\frac{f_s}{2}} K_\eta \cdot \mathcal{H}_2\{T_i\}, \tag{7}$$

where $\theta_{\eta_i}^{\text{rms}}$ denotes the rms pointing jitter due to sensor noise on axis $i$, and $\mathcal{H}_2(T_i)$ represents the white-noise-induced energy norm [21] of $T_i$. Since the budget for $\theta_{\eta_i}^{\text{rms}}$ in Table II translates to 4.7 $\mu$rad rms per axis, and $f_s = 20$ kHz, this implies that the controllers $C_i$ should be such that

$$\mathcal{H}_2\{T_i\} \leq 0.17. \tag{8}$$

For ease of implementation, the controllers $C_i$ have been chosen identical, i.e. $C_x = C_y$, and their bandwidth has been maximized (where higher bandwidths typically yield larger $\mathcal{H}_2\{T_i\}$) for vibration-attenuation reasons, while satisfying condition (8). Fig. 10 shows the obtained frequency responses of the full closed-loop $T$ (including cross-terms) after controller design, using various measurements of $H$ along different QC spot positions. The maximum $\mathcal{H}_2$-norm in $\theta_x$ (first diagonal) is 0.150, and in $\theta_y$ (second diagonal) 0.161, and therefore compliant with the constraint. Moreover, note that the off-diagonals in $T$ are significantly smaller than the diagonals, demonstrating negligible cross-talk, which justifies the original assumption of ignoring the interaction between the axes.

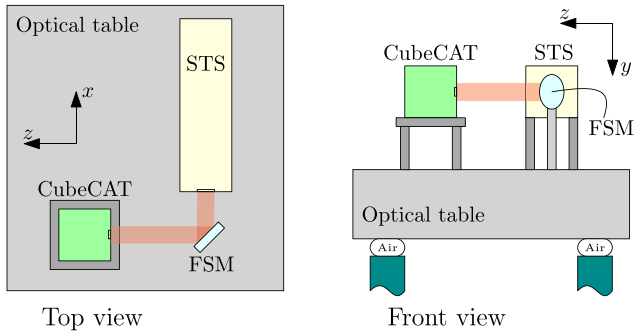


Fig. 12. Illustration of the motion attenuation verification experiment, in which the angle-of-arrival of a several-cm-wide flat-top beam, created by the space terminal simulator (STS), is dynamically perturbed by an external FSM, and the closed-loop transfer function between this angular perturbation and the QC response has been explicitly measured.

### D. Satellite Motion Specification

For an infinitely stiff terminal, or up to its first eigenfrequency, satellite motions influence the pointing performance in the same way as beam angle-of-arrival fluctuations do, which can be seen as the propagation of signals $r_i$ to $\theta_i$ in Fig. 9, determined by the sensitivity transfer function

$$S(s) = \frac{H(s)C(s)}{1 + H(s)C(s)}, \quad \text{with } C(s) = \text{diag}\,(C_x, C_y)\,. \tag{9}$$

This function can thus be used to analyze the micro-vibration attenuation capabilities of a terminal in the low- to mid-frequency range. Fig. 11 shows the frequency response $S(f)$ of this sensitivity for the controller design of Section IV-C in blue, showing a clear attenuation of motions at low frequencies. This performance has been verified explicitly in a dedicated experiment, illustrated in Fig. 12, where an external FSM is used to apply dynamic (white noise) angle-of-arrival disturbances at the CubeCAT aperture, and the frequency response from this

perturbation to the closed-loop QC response has been determined. These results are shown in red in Fig. 11, which matches the designed performance in blue very well. The two responses start to deviate at higher frequencies, which can be attributed to the test setup itself; as visualized in Fig. 12, the setup had to be elevated above the optical table due to practical constraints, and as such the external FSM had to be mounted on a metal post. The eigenfrequencies of this assembly show up as high-frequency modes in Fig. 11, and can therefore be ignored.

To derive specifications for acceptable satellite motion the black dashed lines in Fig. 11 are used, which are lower limits of the attenuation performance, as we can write

$$|S_i(f)| \leq \begin{cases} A_1 \cdot 2\pi f, & \text{for } f < 120\,\text{Hz} \\ A_2, & \text{for } f \geq 120\,\text{Hz} \end{cases} \tag{10}$$

where $A_1 = \frac{1}{380}$ and $A_2 = 2$ describe the dashed lines, and $i$ denotes the first ($x$) or second ($y$) diagonal element. These lines intersect at 120 Hz, which therefore defines the separation between low- and high-frequency in Table II. Below 120 Hz it implies that the PSD of the pointing jitter $P_{\theta_i}(f)$ due to motional disturbances $P_{r_i}(f)$ can be approximated by

$$\begin{aligned} P_{\theta_i}(f) &= |S_i(f)|^2 P_{r_i}(f) \\ &\leq A_1^2 (2\pi f)^2 \cdot P_{r_i}(f) = A_1^2 \cdot P_{\dot{r}_i}(f), \end{aligned} \tag{11}$$

where $P_{\dot{r}_i}$ denotes the PSD of the velocity of the disturbance. The rms pointing due to motional disturbances then satisfies

$$\begin{aligned} \theta_{r_i}^{\text{rms}} &= \sqrt{\int_0^{f_s/2} P_{\theta_i}(f)\,\mathrm{d}f} \\ &\leq \sqrt{A_1^2} \cdot \sqrt{\int_0^{f_s/2} P_{\dot{r}_i}(f)\,\mathrm{d}f} = A_1 \cdot \dot{r}_i^{\text{rms}}, \end{aligned} \tag{12}$$

where $\dot{r}_i^{\text{rms}}$ denotes the rms velocity of the motional disturbance. Using the requirements of Table II, this implies that the pointing budget due to satellite motion will be met as long as

$$\dot{r}_i^{\text{rms}} \leq \frac{\theta_{r_i}^{\text{rms}}}{A_1} = 380\,/\text{s} \cdot 5\,\mu\text{rad} = 1.9\,\text{mrad/s rms}, \tag{13}$$

in other words, as long as all satellite motions up to 120 Hz are less than 1.9 mrad/s rms in *any* direction.

A similar approach can be used for the high-frequency range, which leads to an angular specification of:

$$r_i^{\text{rms}} \leq \frac{\theta_{r_i}^{\text{rms}}}{A_2} = \frac{1}{2} \cdot 5\,\mu\text{rad} = 2.5\,\mu\text{rad rms}, \tag{14}$$

in *any* direction for frequencies above 120 Hz. These specifications have been communicated with the satellite manufacturer, who assessed the NorSat-TD satellite to be compliant with these numbers. As this was not considered a risk, no explicit satellite-level verification tests have been carried out afterwards.

### E. Acquisition Strategy

CubeCAT relies on the body pointing of the satellite for its coarse acquisition, and is designed to confidently deal with body pointing errors of up to ±13 mrad. Knowledge of the body pointing error can be forwarded from satellite to CubeCAT for open-loop correction of the FSM angle, although this is not critical for successful acquisition (and also not used during in-orbit tests). Body pointing of NorSat-TD is based on GPS-data of the satellite and the ground station, and is handled by NorSat-TD itself.

The relatively large FoV of the CubeCAT tracking sensor implies that it can detect misalignments between angle-of-arrival and the terminal boresight of up to ±6 mrad, i.e. about half of the acceptable body pointing error. This allows for a baseline non-spiral acquisition mode in which the CubeCAT feedback loop will simply be switched on once the QC detects a total intensity of more than 0.4 nW (its functional threshold), so that the controlled FSM will pull the spot on the QC towards the center. In the ±0.6 mrad linear QC regime this response will be in accordance with the bandwidth shown in Fig. 10 (few tenths of ms), outside this regime the response is somewhat slower due to sensor saturation.

Still, the accumulation of various uncertainties, including Tx/Rx-misalignment, misalignment between CubeCAT and the satellite, hysteresis in the FSM, and satellite body pointing errors, could possibly exceed the 6 mrad FoV. For this reason, an additional backup spiral acquisition routine has been implemented. Constant angular velocity spiral setpoints have been programmed, together with a static feedforward, to repeatedly spiral the FSM in open-loop to effectively use the FSM range and artificially increase the FoV. Once a spot appears on the QC, with an intensity exceeding 0.4 nW, the spiral is aborted and the feedback loop is switched on, pulling the spot to the QC center. Nominally, the FSM spirals with 12 Hz and 3 mrad pitch,[3] in which case a uncertainty cone is covered in just 1 s (for a complete out- and inward spiral).

## V. Laboratory Verification Tests

CubeCAT has been extensively tested in laboratory environments. The main outcomes are discussed in this section.

### A. Opto-Mechanical Tests

On the basis of the optical and mechanical architecture as discussed in Sections III-A and III-B, key properties of the CubeCAT system have been tested. With respect to Tx beam divergence (88.5 μrad), optical bench Tx transmission (0.882) and laser source power (0.3 W) compliant performance has been demonstrated. Note that during the in-orbit link experiments, the output power has been set to 278 mW. As for the critical co-alignment of Tx and beacon (Rx) beams an error of 0.07 mrad has been measured, which is well within specification. The stability of this co-alignment amounts to 27 μrad (3$\sigma$ value), which is slightly above the requirement of 20 μrad.

### B. Pointing Performance Verification

The pointing performance of CubeCAT has been verified in a series of tests, each focusing on specific contributors to the

[3] All software parameters can be updated in orbit, so faster or smaller-pitched spirals can also be selected if desired.

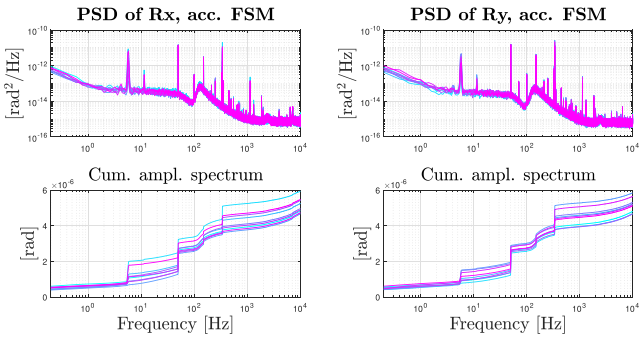


Fig. 13. Spectra of the closed-loop pointing jitter with the minimal optical power of 0.8 nW on the QC, as measured by the (temporarily) installed FSM sensors, both for $\theta_x$ (left) and $\theta_y$ (right). Different colors represent different repeated measurements over time.

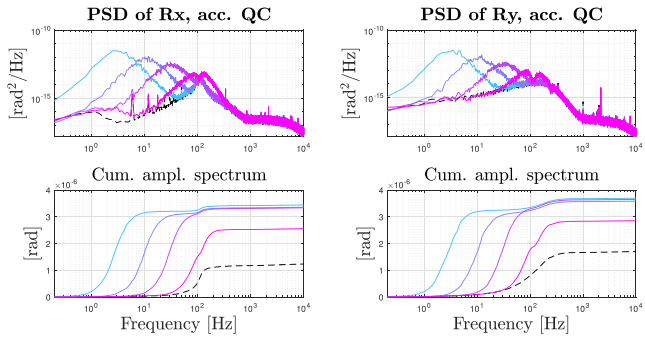


Fig. 14. Pointing jitter as measured by the QC with 40 nW of optical power, with 1.9 mrad/s rms of additional optical perturbation in either the 3.0 Hz–3.3 Hz (—), 10 Hz–11 Hz (—), 30 Hz–33 Hz (—), or 100 Hz–110 Hz (—) frequency range; the black dashed line indicates the pointing jitter without additional perturbation.

overall pointing budget. First, the propagation of QC sensor noise has been verified in a set-up similar to the one shown in Fig. 12, but with the external FSM replaced by a fixed static mirror. CubeCAT is set into closed-loop using the controller described in Section IV-C, subject to a stationary angle-of-arrival flat-top Rx-beam with an intensity of 0.8 nW at the QC. The internal FSM in CubeCAT was temporarily equipped with sensors to measure the actual (feedback-induced) FSM angles. The PSDs of this FSM motion, representing the Tx jitter, are shown in Fig. 13. Since this experiment is sensor-noise dominated, these PSDs have a similar shape as $T_i(f)$ in Fig. 10, complemented by some known FSM sensor artifacts such as the noise floor at high frequencies and a tone at 50 Hz. When these sensor effects are subtracted from the cumulative spectrum, the observed jitter is between 3.0 and 4.7 $\mu$rad rms on both $\theta_x$ (left) and $\theta_y$ (right), which is compliant with the QC noise budget in Table II.

To verify the pointing performance subject to satellite motion the same setup as in Fig. 12 has been used, i.e. with a moveable external FSM, and while CubeCAT was in closed-loop with 40 nW of power on its QC. In a sequence of tests this external FSM was perturbed randomly with different band-pass filters leading to 1.9 mrad/s rms of motion: 3.0 Hz–3.3 Hz, 10 Hz–11 Hz, 30 Hz–33 Hz, and 100 Hz–110 Hz, where lower frequencies naturally lead to larger angular amplitudes. The PSDs of the resulting pointing, as measured by the QC, are shown in Fig. 14. The dashed lines represent the case without added bandpass perturbation, hence the rms increase with respect to this benchmark is the pointing deterioration due to angular disturbances. This increase is less than 3.2 $\mu$rad rms per axis, and less than 4.5 $\mu$rad rms in total, which is within the 5 $\mu$rad rms satellite motion budget of Table II.

### C. Acquisition Verification

The acquisition capabilities of CubeCAT have been verified explicitly using again the set-up illustrated in Fig. 12. To this end, the external FSM has been set to 1000 different randomly selected static angles to simulate 1000 different random initial angles-of-arrival between 4 and 18 mrad, after which CubeCAT was switched on to determine its acquisition success and speed. The results are shown in Fig. 15, which indicates that 45% of

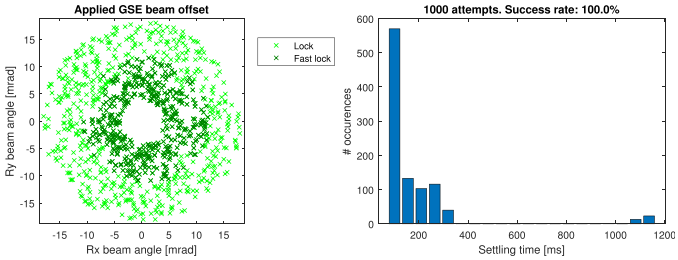


Fig. 15. Summary of 1000 acquisition tests, where each cross in the left plot represents a test with a random initial angle-of-arrival between 4 and 18 mrad, representing either immediate successful acquisition without spiraling (dark green), acquisition needing some level of spiraling light green), and unsuccessful acquisition (red, absent). The histogram on the right shows the associated acquisition times, where the settling time is stringently defined by how long it takes for the pointing error to stay within just $\pm 40$ $\mu$rad.

these tests settle without spiraling within 75 ms to an error of less than $\pm 40$ $\mu$rad, 51% of the tests need some degree of spiraling to settle within at most 350 ms, while only 4% need a little more than one complete spiral, hence more than 1 s, to successfully lock. None of the tests have failed, which demonstrates the success of both the baseline and spiral acquisition modes.

## VI. In-Orbit Tests and Data Analysis

The CubeCAT terminal has been installed at the NorSat-TD satellite, which was launched on April 15, 2023 into a sun-synchronous orbit at 500 km height. After a successful commissioning phase, the first attempts to establish actual links started in July 2023. This section describes the results of various successful downlinks between CubeCAT and three optical ground stations.

In the overview in Table III, the optical links with the CubeCAT terminal are listed. Here, the number of optical links is specified with the time period they have occurred in, the time of day, the time needed for acquisition and the duration of the links. From data communication perspective, the number of actual (1 Gbit/s) data downlinks is specified. Up to now, there are no numbers available for overall data volumes transferred.

TABLE III
ESTABLISHED LINKS CUBECAT - OGS

| | *TNO OGS (The Hague)* | *MeO (Grasse)* | *Izaña-1 (Tenerife)* |
|---|---|---|---|
| period | 10 Jan 2024 - 12 Apr 2025 | 5-17 Dec 2024 | 18 Nov 2023 - 4 Dec 2024 |
| # optical links | 12 | 6 | 11 |
| time of day | day and night | day and night | day and night |
| acquisition time | 10-30 s | number not available | 5-16 s |
| link duration | 48-195 s | 60-302 s | 15-148 s |
| # data links | 6 | 4 | number not available |

### A. The TNO OGS in the Hague

The main OGS for the CubeCAT downlink tests is the TNO OGS in The Hague. This test facility is located at a $45\,\mathrm{m}$ high tower at sea level in The Hague and was developed for performing DTE laser communication experiments [22]. The OGS consists of an $800\,\mathrm{mm}$ Ritchey-Chretien telescope and the Gigabit Optical Communications Active Terminal (named GoCAT) ground terminal. GoCAT has been developed using commercial off-the-shelf components for bi-directional communication with LEO satellites up to 10 Gbit/s. Next to the OGS a Miratlas SkyMonitor is located on the tower for measuring the encountered atmospheric conditions.

For the beacon uplink from GoCAT to CubeCAT onboard the NorSat-TD satellite, the link budget can be summarized as follows. With $7.1\,\mathrm{W}$ laser power at GoCAT a large loss margin is available given the $0.8\,\mathrm{nW}$ threshold at the CubeCAT detector. For a satellite orbit at $500\,\mathrm{km}$ height, an elevation angle of $20^\circ$, a relatively high Tx-beam divergence of $220\,\mu\mathrm{rad}$ and the CubeCAT Rx aperture of $17\,\mathrm{mm}$, the geometrical loss amounts to 86.8 dB. Then, allowing for a total of 7 dB atmospheric losses (turbulence-induced and attenuation), 2 dB pointing losses and 3 dB aggregate transmission loss at Tx and Rx, still yields a power level above the $0.8\,\mathrm{nW}$ threshold of the CubeCAT detector.

### B. In-Orbit Pointing Performance Verification in Link With TNO OGS the Hague

The first time both the The Hague OGS and CubeCAT have seen and recorded light from the counter-terminal was on January 10, 2024. During an overpass with $56^\circ$ maximum elevation, the $17\,\mathrm{s}$ tracing file recorded by CubeCAT captured the switch from open to closed-loop, as can be seen in the received QC intensity in the top plot in Fig. 16, which occurred before culmination at around $44^\circ$ elevation. There is a sudden blip on the QC intensity around $t = 2\,\mathrm{s}$ due to the spiraling of the OGS, after which CubeCAT closes its feedback loop; shortly thereafter the OGS stops spiraling due to the detection of the CubeCAT laser, so that from $t = 2.8\,\mathrm{s}$ onward the CubeCAT pointing is constantly actively controlled, leading to high intensity levels on the QC and a strong reduction of the pointing error (bottom plot).

The inlay on the top plot of Fig. 16 shows the probability density function (PDF) of the received intensity, and displays a close-to log-normal distribution, with a mean received power of $16.4\,\mathrm{nW}$ and a standard deviation of $7.4\,\mathrm{nW}$, which is much higher than the minimally budgeted $0.8\,\mathrm{nW}$. The high QC

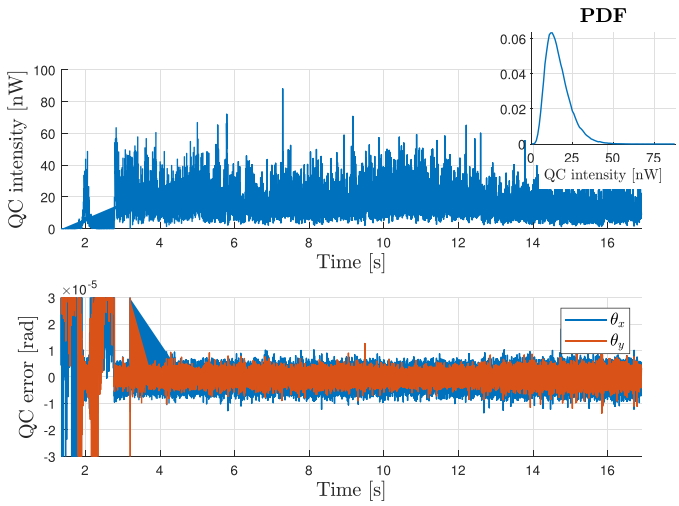


Fig. 16. Recorded CubeCAT time traces of mission 605068 (17 s at 20 kHz), showing the measured intensity at the QC and its PDF (top) and the tip/tilt pointing jitter (bottom).

intensity implies that the sensor noise on $\theta_x$ and $\theta_y$ in the bottom of Fig. 16 is fairly low for this overpass. The observed pointing jitter is only $2.4\,\mu\mathrm{rad}$ and $1.5\,\mu\mathrm{rad}$ rms in $\theta_x$ and $\theta_y$ respectively, which translates to a pointing error with mean $\mu_p = 2.4\,\mu\mathrm{rad}$ and standard deviation $\sigma_p = 1.5\,\mu\mathrm{rad}$ (omitting possible static misalignments which are unobservable in these measurements). This demonstrates that CubeCAT is pointing much more precisely than originally budgeted for, which has a positive effect on the link budget.

### C. Verification of Received Irradiance Levels in Downlink Data

The mean irradiance and irradiance fluctuations have been analyzed on the basis of the models in [15], [16]. For the specific contributions of pointing error, atmospheric fading and atmospheric attenuation the approaches as described below have been followed.

*1) Pointing Error:* The boresight pointing error is determined by both the point-ahead angle (PAA) and the angular offset between the Tx and Rx beam on the CubeCAT terminal. During the measurements the PAA compensation mechanism was turned off and hence the PAA-induced boresight error is fully accounted for in the model. For the residual Tx-Rx angular offset a value of $15\,\mu\mathrm{rad}$ has been adopted. For the pointing

jitter, the values as discussed in the previous section have been used.

*2) Turbulence-Induced Scintillation:* An estimate of the actual $C_n^2$-profile is obtained by fitting the two parameters in the HV-5/7 model to measurements of the scintillation index and the Fried parameter, performed at the ground station. The von Kármán power spectrum is then used to evaluate the log-amplitude fluctuations; see (1).

*3) Atmospheric Attenuation:* The cloud-free atmospheric extinction around $1545\,\mathrm{nm}$ consists of a molecular absorption and an aerosol absorption and scattering contribution. The molecular absorption in turn consists of water vapor and carbon dioxide component, whereas the aerosol's contribution to the extinction is assumed to be of rural nature. An estimate of the loss induced by atmospheric extinction is calculated using the line-by-line algorithm of the MODerate resolution atmospheric TRANsmission (MODTRAN) code [14]. MODTRAN computes line-of-sight atmospheric spectral transmittances and radiances in built-in or user-defined atmospheres by defining the required meteorological, molecular and aerosol parameters on several atmospheric altitude layers.

To calculate the molecular absorption, MODTRAN relies on the HITRAN database [23]. Apart from humidity and carbon dioxide profiles, pressure and temperature conditions are of importance for the calculation of the molecular absorption, as these determine the pressure and temperature broadening of the absorption lines. Given the location of the measurements and the time at which they were obtained, we referred to the built-in profile designated by 'mid-latitude winter' to define representative conditions for meteorology and carbon dioxide $CO_2$. For the aerosol condition the built-in model designated by 'rural' is used, which is representative for continental areas which are not influenced by urban or industrial sources. It consists of 70% water soluble substance and 30% dust, both represented by different size distributions. MODTRAN allows to scale the amount of those substances with a visibility, thereby making the aerosol extinction estimates more representative of the actual conditions at play during the measurements. To evaluate the actual atmospheric attenuation at the time of the downlink measurements, the MODTRAN calculations have been fed by visibility data from measurements near the OGS.

Note that the irradiance values shown in Figs. 17 and 18 presented below have been derived from a free-space power detector output, and converted to irradiance at telescope aperture level by accounting for the transmission losses and the actual telescope aperture areas.

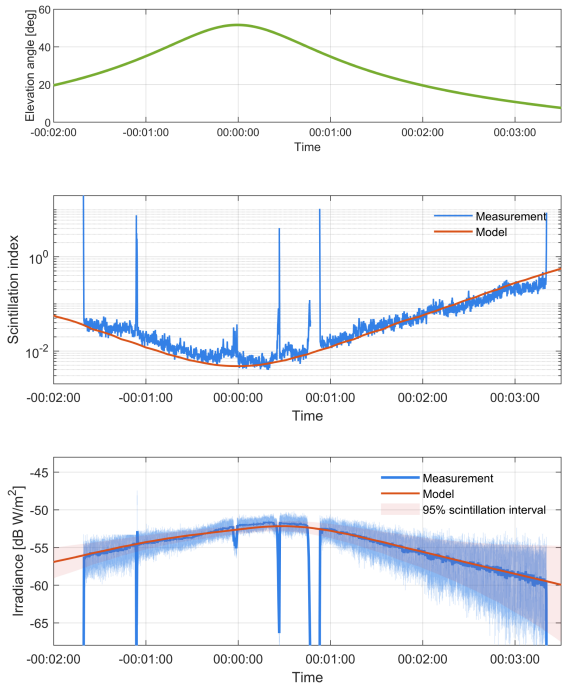


Fig. 17. Measured and modeled MeO receiver data for 6 December 2024; elevation angle (top), irradiance scintillation index (middle) and received irradiance (bottom).

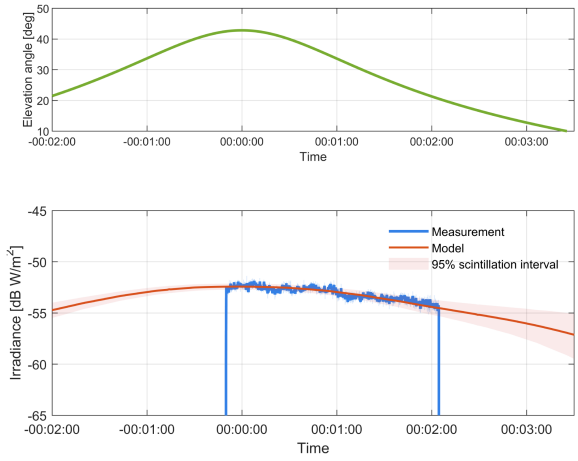


Fig. 18. Measured and modeled ESA OGS receiver data at Izaña for 25 November 2023; elevation angle (top) and received irradiance (bottom).

### *D. Downlink Test to Optical Metrology Laser Station (MeO), France*

The MeO telescope was initially designed for laser-ranging, but was later extended for other scientific objectives, including laser satellite communication experiments [24]. MeO is located near Grasse, France, at 1270 meters above the sea level and is based on a 1.54 m Ritchey-Chretien telescope. The experiments with CubeCAT have been conducted with Géoazur and Centre National d'études Spatiales (CNES) under a cooperation agreement between Norwegian Space Agency (NOSA) and CNES, as a follow up of previous campaigns performed with the Grasse station. During this test campaign, two links of 5 minutes have been established, which basically cover a full overpass [25]. During the experiments, the atmospheric conditions have been monitored by the Moon Limb Profiler (PML) [26] and Generalized Differential Image Motion Monitor (GDIMM) [27]. In Fig. 17 the model and measured irradiance levels and scintillation are shown. It reveals relatively low scintillation levels (as expected) and good agreements between model and measurements.

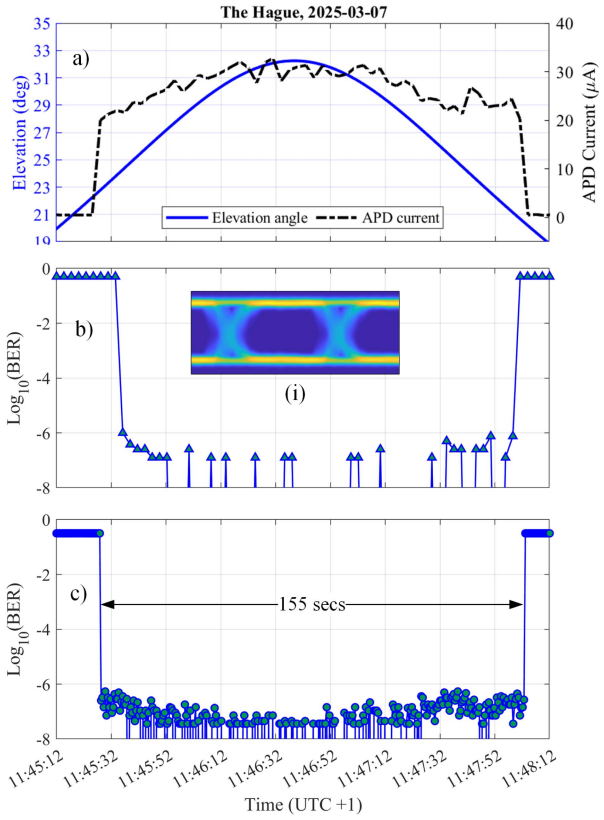


Fig. 19. Plots of the (a) APD detector current and elevation angle, (b) BER performance based on post-processed data recorded by the oscilloscope and (c) BER performance of the data as stored by the ground station modem. Inset (i) is the eye diagram at error-free link time.

TABLE IV
MAIN CUBECAT SYSTEM PROPERTIES - REQUIREMENTS VERSUS TESTS

| *Parameter* | *Required Value* | *Test outcome* |
|---|---|---|
| Key performance | | |
| Tx data rate | ≥1 Gbit/s | 1 Gbit/s, with BER ($\leq 10^{-6}$). |
| Recurring production cost | ≤50 kEUR | commercial in confidence |
| Power consumption | ≤30 W | 10.8 W |
| Volume | $0.1 \times 0.1 \times 0.1$ m$^3$ | $0.1 \times 0.1 \times 0.1$ m$^3$ |
| Volume with suspension module | | $0.15 \times 0.14 \times 0.12$ m$^3$ |
| Mass | ≤1.33 kg | 1.0 kg |
| Mass with suspension module | ≤2.31 kg | 2.11 kg |
| Lifetime | ≥ 4 years | 2.1 years (aborted by satellite decay) |
| Operational | | |
| Satellite orbits | 300 – 900 km | 367 – 500 km |
| Link Range | up to 1200 km | up to 1550 km |
| Elevation angle | ≥20° | ≥9° |
| Environmental | | |
| space conditions | low Earth orbit | operational terminal |
| launch conditions | Falcon-9 vehicle | operational terminal |

### E. Downlink Test to ESA Ground Station At Tenerife

The European Space Agency (ESA) ground station Izaña-1 (IZN-1) is a laser ranging station in Tenerife [28], which is used as a test bed for laser communication. IZN-1 is located at the Teide Observatorium, 2400 m above sea level and is fitted with an 800 mm Ritchey-Chretien telescope. The ground station was developed by DiGOS GmbH and can be operated fully remotely. Near IZN-1 a Miratlas SkyMonitor is located to monitor the turbulence conditions during the experiments. The comparison between model and measured irradiance traces at the receiver is given in Fig. 18. Again, a close match can be observed.

### F. Downlink Communication Performance at the Hague OGS

For the The Hague OGS, Fig. 19 shows the results of the successful 1 Gbit/s downlink on March 07, 2025 with the key set-up configurations described in Section III-C. The optical link has been established at an elevation angle of 22.5°, with a peak at 32°, and has been lost when the elevation decreased to 20.5°. The corresponding APD photo-currents are approximately 20 $\mu$A, 33 $\mu$A, and 20 $\mu$A, respectively. These correspond to (average) received optical power levels of approximately −31 dBm and −29 dBm, respectively. As may be expected, the results show lower received optical powers associated with lower elevation angles, caused by a combination of additional geometric, extinction and turbulence-induced losses.

Fig. 19(b) and (c) show the BER measurements for the downlink signal, as 1) sampled and post-processed with a real-time oscilloscope and 2) digitized and stored by the OGS modem, respectively. After the data link was acquired, both methods consistently achieved BERs below $1 \times 10^{-6}$ without error correction. Note that an error floor between $1 \times 10^{-6}$ and $1 \times 10^{-7}$ has also been measured during the verification tests of CubeCAT in the lab and is caused by the transmit signal quality of the directly modulated laser. The inset in Fig. 19(b) presents a typical OOK eye diagram acquired during the overpass, at a time when the link was error-free, visualized as BER below $1 \times 10^{-8}$. The active link duration is approximately 155 seconds. Note that no error-correction technique was applied in this experiment.

### G. Review of Requirements and Test Results

In Section II the key requirements for the CubeCAT terminal have been outlined. Given the outcomes of laboratory tests and the successful in-orbit link experiments, the measure of compliance can be assessed. In Table IV this comparison is listed. Most of the key requirements have been met and the in-orbit test results have confirmed the feasibility of the main CubeCAT system performance parameters.

## VII. CONCLUSION

The CubeCAT optical communication terminal for small satellites is suited for 1 Gbit/s data rate in downlinks from LEO orbits. It has a 1U volume, 1.0 kg mass and 10.8 W power consumption. For this LEO satellite terminal a feasible link budget has been presented. The optical architecture is compact and contains a low number of components and is photon-efficient. The mechanical structure has low mass and highly stable behavior. For survival of severe launch vibrations and shock, a dedicated suspension module can be added. The communication approach is compliant with the CCSDS O3K standard.

The pointing control strategy has demonstrated high performance in reducing the jitter towards negligible levels, while keeping the QC sensor noise-induced error bounded. The link acquisition strategy has proven to operate fast and reliably. For downlinks from CubeCAT to two optical ground stations the received irradiance levels have been verified with the optical link models for a large range of elevation angles. Ultimately, a 1 Gbit/s data rate from CubeCAT to the The Hague OGS has been demonstrated with a low BER ($\leq 10^{-6}$).

## ACKNOWLEDGMENT

The TNO team would like to explicitly thank its partners, without whom this demonstration and the subsequent results would not have been possible. With respect to CubeCAT this includes AAC Clydespace Hyperion and Gooch&Housego for their contribution to the hardware, and NOSA, StatSat AS and the University of Toronto Institute for Aerospace Studies - Space Flight Laboratory (UTIAS-SFL) for the launch opportunity and mission support. The CubeCAT terminal is currently manufactured in series by AAC Hyperion and FSO Instruments, and its FSM by Demcon. The development of CubeCAT is supported by the Netherlands Space Office (NSO) and jointly funded by ESA ARTES Strategic Programme Line ScyLight, Netherlands Ministry of Defense and TNO, together with the companies involved in the project.

For the The Hague ground station the partners include Airbus-NL, ASA Astrosysteme GmbH, Celestia STS and DiGOS Potsdam GmbH. For the MeO ground station: Geraldine Artaud (CNES), Julien Chabé and Duy-Ha Phung (both Géoazur), Etienne Samain (SigmaWorks) and Alain Thomas (Safran data systems). For the Izaña ground station: Nick Champion, Andrea Di Mira and Clemens Heese from the European Space Operations Centre (Germany).

The authors would like to share their appreciation to all (former) TNO colleagues for the design, manufacturing, testing and experiments with CubeCAT.

## REFERENCES

[1] N. J. Nzekwu, M. A. Fernandes, G. M. Fernandes, P. P. Monteiro, and F. P. Guiomar, "A comprehensive review of UAV-assisted FSO relay systems," *Photonics*, vol. 11, no. 3, 2024, Art. no. 274.

[2] G. K. Kurt et al., "A vision and framework for the high altitude platform station (HAPS) networks of the future," *IEEE Commun. Surv. Tuts.*, vol. 23, no. 2, pp. 729–779, Secondquarter 2021.

[3] D. R. Kolev et al., "Latest developments in the field of optical communications for small satellites and beyond," *J. Lightw. Technol.*, vol. 41, no. 12, pp. 3750–3757, Jun. 2023.

[4] A. Carrasco-Casado et al., "Leo-to-ground optical communications using sota (small optical transponder)–payload verification results and experiments on space quantum communications," *Acta Astronautica*, vol. 139, pp. 377–384, 2017.

[5] C. Fuchs and C. Schmidt, "Update on DLR's OSIRIS program," *Proc. SPIE*, vol. 11180, 2019, Art. no. 111800I.

[6] C. M. Schieler et al., "TBIRD 200-Gbps CubeSat downlink: System architecture and mission plan," in *Proc. IEEE Int. Conf. Space Opt. Syst. Appl.*, 2022, pp. 181–185.

[7] S. V. Weston et al., "State-of-the-art of small spacecraft technology," NASA/TP—20250000142, Feb. 2024, Accessed: Apr. 14, 2025. [Online]. Available: https://www.nasa.gov/wp-content/uploads/2025/02/soa-2024.pdf

[8] M. Dresscher et al., "Key challenges and results in the design of CubeSat laser terminals, optical heads and coarse pointing assemblies," in *Proc. IEEE Int. Conf. Space Opt. Syst. Appl.*, 2019, pp. 1–6.

[9] M. Milaševičius and L. Mačiulis, "A review of mechanical fine-pointing actuators for free-space optical communication," *Aerospace*, vol. 11, no. 1, 2024, Art. no. 5. [Online]. Available: https://www.mdpi.com/2226-4310/11/1/5

[10] S. Kuiper et al., "High-bandwidth and compact fine steering mirror development for laser communications," in *Proc. 17th Eur. Space Mechanisms Tribol. Symp.*, 2017.

[11] G. Witvoet et al., "Performance validation of a high-bandwidth fine steering mirror for optical communications," in *Proc. SPIE*, Z. Sodnik, N. Karafolas, and B. Cugny, Eds., International Society for Optics and Photonics: SPIE, vol. 11180, 2019, Art. no. 1118061, doi: 10.1117/12.2536136.

[12] R. Sasiela, *Electromagnetic Wave Propagation in Turbulence* - 2nd ed. Bellingham, WA, USA: The Society of Photo-Optical Instrumentation Engineers, 2007.

[13] B. J. Klein and J. J. Degnan, "Optical antenna gain. 1: Transmitting antennas," *Appl. Opt.*, vol. 13, no. 9, pp. 2134–2141, 1974.

[14] A. Berk, L. S. Bernstein, and D. C. Robertson, "MODTRAN: A moderate resolution model for LOWTRAN," Scientific Rep. 1, Spectral Sci. Inc., Burlington, 1987.

[15] A. A. Farid and S. Hranilovic, "Outage capacity optimization for free-space optical links with pointing errors," *J. Lightw. Technol.*, vol. 25, no. 7, pp. 1702–1710, 2007.

[16] F. Yang, J. Cheng, and T. A. Tsiftsis, "Free-space optical communication with nonzero boresight pointing errors," *IEEE Trans. Commun.*, vol. 62, no. 2, pp. 713–725, Feb. 2014.

[17] N. Doelman, G. Witvoet, E. Veldhuis, S. Langedijk, and K. Broekens, "Non-stationary irradiance properties in dynamic FSO links: A model and field tests study," *Proc. SPIE*, vol. 13194, 2024, Art. no. 131940J .

[18] R. Saathof et al., "Optical satellite communication space terminal technology at TNO," *Proc. SPIE*, vol. 11180, 2019, Art. no. 111800K.

[19] W. Gielesen et al., "Gaia basic angle monitoring system," *Proc. SPIE*, vol. 8442, 2012, Art. no. 84421R.

[20] F. van Kempen, J. de Vreugd, and W. Crowcombe, "Device for mounting a load to carrier, assembly, VEHICLE and methods," the Netherlands Patent WO2021206552A1, Apr. 8, 2021. [Online]. Available: https://worldwide.espacenet.com/

[21] S. Skogestad and I. Postlethwaite, *Multivariable Feedback Control: Analysis and Design*. Chichester, U.K.: John Wiley, 2005.

[22] G. Witvoet, D. de Bruijn, S. Redi, R. Herfst, and C. Korevaar, "First-light results of the in-orbit demonstration of a CubeSat-compatible optical communication terminal," *Proc. Int. Conf. Space Optics—ICSO*, vol. 13699, 2024, Art. no. 1369907. [Online]. Available: https://doi.org/10.1117/12.3075383

[23] I. E. Gordon et al., "The hitran2020 molecular spectroscopic database," *J. Quantitative Spectrosc. Radiative Transfer*, vol. 277, 2022, Art. no. 107949.

[24] E. Samain et al., "First free space optical communication in Europe between SOTA and MEO optical ground station," in *Proc. IEEE Int. Conf. Space Opt. Syst. Appl.*, 2015, pp. 1–7.

[25] K. Broekens et al., "In-orbit test results of a free space optical satellite link between a CubeSat-compatible laser communication terminal and MeO ground station," *Proc. SPIE*, vol. 13355, 2025, Art. no. 1335508.

[26] E. Aristidi et al., "A generalized differential image motion monitor," *Monthly Notices Roy. Astron. Soc.*, vol. 486, no. 1, pp. 915–925, 2019.

[27] J. Chabé et al., "PML: A generalized monitor of atmospheric turbulence profile with high vertical resolution," *Appl. Opt.*, vol. 59, no. 25, pp. 7574–7584, 2020.

[28] S.-u. Alam et al., "Beacon system for ESA IZN-1 optical ground station," in *Proc. IEEE Int. Conf. Space Opt. Syst. Appl.*, 2022, pp. 138–141.

**Niek Doelman** (Member, IEEE) received the M.Sc. (*cum laude*) and Ph.D. degrees in applied physics from the Delft University of Technology, Delft, The Netherlands. He is currently a Principal Scientist with TNO High Tech Industry and Professor by special appointment with the Control System Technology section, Eindhoven University of Technology, Eindhoven, The Netherlands. His research interests include the control of optical waves, for the applications of optical wireless communication, ground-based astronomy, and space science.

**Gert Witvoet** (Member, IEEE) received the M.Sc. (*cum laude*) and Ph.D. degrees from the Eindhoven University of Technology, Eindhoven, The Netherlands, in 2007 and 2011, respectively. He is currently a Senior Dynamics and Control Specialist with the Netherlands Organisation for Applied Scientific Research, Delft, The Netherlands, and a part-time Associate Professor with Mechanical Engineering Department, the Eindhoven University of Technology. His research interests include advanced motion and learning control for high-tech instruments for the semiconductor, astronomy, and space markets.

**Dick de Bruijn** is currently a Lead Researcher of optical engineering with TNO High Tech Industry. Hisresearch interests include space terminals and ground stations for optical satellite communication, since 2018.

**Arjo Bos** received the Ph.D. degree in mechanical engineering degree, specializing in precision engineering, from the Eindhoven University of Technology, Eindhoven, The Netherlands, in 2017. He is currently a Senior Mechanical Architect and Mechanical Expertise Lead with TNO's Optomechatronics Department, Delft, The Netherlands, mainly working on challenges in laser satellite communication and ground-based astronomy.

**Arnoud Delissen** received the Ph.D. degree in mechanical engineering from the Delft University of Technology, Delft, The Netherlands, in 2022. He is currently with TNO on topology optimization for various applications.

**Dong-Nhat Nguyen** received the Ph.D. degree in electrical engineering from The University of Nottingham, Semenyih, Malaysia, in 2018. He is currently an Optical Communications Engineer with TNO High Tech Industry, Delft, The Netherlands. His research focuses on integrated radio optical communications.

**Loes Scheers** received the M.Sc. degree in physics and astronomy from Radboud University, Nijmegen, The Netherlands, in 2017. Since 2018, she has been a Scientist with the Department of Electronic Defence, TNO, focusing on the visibility of naval platforms and the radiative transfer and propagation of electromagnetic waves for a multitude of applications. Her strength resides in modelling. She is currently actively involved in research on modeling atmospheric state details relevant for free-space optical communication links, with a focus on optical turbulence.

**Hedser van Brug** received the Ph.D. degree from the free university of Amsterdam, Amsterdam, The Netherlands, in 1988, on the topic of soft X-ray spectroscopy. His professional career started with the Delft University of Technology, Delft, The Netherlands, where he was an Associate Professor, till 2001, when he switched to working with TNO, Delft, as Optical Designer. His research interests include earth observation satellites, communication satellites, and medical instruments. Besides the actual optical design, also thin layer design and stray light analysis are parts of his daily research.

**Robbert Voorhoeve** received the M.Sc. degree in mechanical engineering (*cum laude*) and applied physics, and the Ph.D. degree in mechanical engineering from the Eindhoven University of Technology, Eindhoven, The Netherlands, in 2013 and 2018, respectively. He is currently a Dynamics and Control Specialist with the Netherlands Organisation for Applied Scientific Research (TNO), Delft, The Netherlands. His research interests include adaptive optics, system identification, and control of complex mechatronic systems.

**Kristiaan Broekens** is currently a Systems Engineer with the Laser Satcom Program of TNO. Apart from the development of next generation terminals he manages the SmallCAT operations, data processing, and model verification.

**Cornelis Willem Korevaar** received the Ph.D. *(cum laude)* degree in electrical engineering *(cum laude)* from the University of Twente, Enschede, The Netherlands. He is currently a Technical Lead of the Optical Satellite Communications Program with the Applied Research Institute TNO and Associate Researcher with Eindhoven University of Technology, Eindhoven, The Netherlands, specializing in laser satellite communications and signal processing.

**Floris van Kempen** received the M.Sc. and Ph.D. degree in mechanical engineering from the Delft University of Technology, Delft, The Netherlands. He is currently a Technical Lead of the Optical Satellite Communications Program with the Applied Research Institute TNO.